Journal of Membrane Science 660 (2022) 120800

Contents lists available at ScienceDirect

Journal of Membrane Science

journal homepage: www.elsevier.com/locate/memsci

The influence of feedwater pH on membrane charge ionization and ion rejection by reverse osmosis: An experimental and theoretical study

E.M. Kimani [a,b], M. Pranić [c], S. Porada [a], A.J.B. Kemperman [a,b], I.I. Ryzhkov [d,e], W.G.J. van der Meer [b,f], P.M. Biesheuvel [a,*]

[a] Wetsus, European Centre of Excellence for Sustainable Water Technology, Oostergoweg 9, 8911 MA, Leeuwarden, the Netherlands
[b] Membrane Science and Technology Cluster, University of Twente, Drienerlolaan 5, 7522 NB, Enschede, the Netherlands
[c] Environmental Technology, Wageningen University, Bornse Weilanden 9, 6708 WG, Wageningen, the Netherlands
[d] Institute of Computational Modeling SB RAS, Akademgorodok 50-44, 660036, Krasnoyarsk, Russia
[e] Siberian Federal University, Svobodny 79, 660041, Krasnoyarsk, Russia
[f] Oasen Drinking Water Company, Nieuwe Gouwe O.Z. 3, 2801 SB, Gouda, the Netherlands

ARTICLE INFO

Keywords:
Reverse osmosis
Desalination
Membrane charge ionization
Multicomponent membrane mass transport
pH-dependence on ion rejection

ABSTRACT

Modeling mass transport of ions across the polyamide active layer of a reverse osmosis (RO) membrane requires a comprehensive understanding of membrane structure and chemistry. For instance, membrane charge ionization and thus salt transport greatly depend on feedwater pH and composition, but these relations are not yet well understood. To address this gap in understanding, a one dimensional model is developed that couples transport of all ions using the extended Donnan steric partitioning pore model. The model includes membrane charge ionization as well as interaction with H^+ and OH^--ions. The dependence of ion rejection and permeate pH is described as function of feedwater pH. Finally, model predictions are quantitatively compared with experimental data by adjusting a few fitting parameters using the Nelder-Mead algorithm. Contrary to other RO studies, we show that the polyamide is only weakly charged, but this small charge still plays a key role to determine membrane performance. These findings reveal the key role of local pH in the ionization of membrane functional groups, and how local charge affects overall membrane rejection of ions as well as permeate pH.

1. Introduction

Globally, the use of reverse osmosis (RO) membrane technology for water desalination has been on a steady rise, currently accounting for ~69% of the total global desalinated water production [1–4]. The RO technology adopts the theory of pressure and chemical potential gradients to achieve selectivity (>99% salt rejection) [5,6]. The most widely used RO membrane is the polyamide thin film composite (PA-TFC) membrane, which consists of two layers: the support layer, and the active layer (Fig. 1). The microporous support layer often is made of polysulfone (~200 μm thickness) and polyester (~150 μm thickness) layers, which provide mechanical strength to the actual membrane. The active layer is made of an ultra-thin (≤200 nm thickness) polyamide (PA) layer, which forms a barrier for salts, i.e., allowing mostly water molecules to go through while significantly retaining salts [7,8].

The polyamide active layer of a TFC-RO membrane is in most cases fabricated by the interfacial polymerization reaction of two monomers; m-phenylenediamine, which is dissolved in the aqueous phase, and trimesoyl chloride, which is solved in the organic phase [9,10]. The highly crosslinked layer contains functional end groups (amine and carboxylic), which can further react [11]. Furthermore, the total membrane charge density, which is determined by these functional groups (FGs), is known to be a function of local pH, which changes across the membrane [12,13]. For instance, at low pH, the amine groups ($R\text{-}NH_2$) easily protonate and acquire a positive charge ($R\text{-}NH_3^+$). Similarly, at high pH, the carboxylic groups (R-COOH) deprotonate and become negatively charged ($R\text{-}COO^-$) [14]. The Donnan electrostatic exclusion (DEE) of ions by the charged FGs at the membrane pore brings about repulsion of the co-ions and attraction of the counter-ions, thus affecting the ion partitioning as shown in Fig. 1 [15]. The ionization of these chemical FGs and their interactions with H^+ and OH^- during desalination of NaCl salt solution at different feed pH and their influence on salt rejection therefore form the focus of this research.

Several mathematical models based on either the solution diffusion

* Corresponding author.
E-mail addresses: e.m.kimani@utwente.nl (E.M. Kimani), Maarten.Biesheuvel@wetsus.nl (P.M. Biesheuvel).

https://doi.org/10.1016/j.memsci.2022.120800
Received 13 May 2022; Received in revised form 28 June 2022; Accepted 5 July 2022
Available online 8 July 2022

theory, the pore flow theory, or molecular dynamics, have been developed to predict water and solute flux across RO membrane [16–20]. However, only a few models have included the effects of membrane charge ionization together with transmembrane flux of H^+ and OH^- -ions into their transport approach. Yet, they influence both ion rejection and permeate pH [21]. Several mechanisms, by which these two ions traverse the membrane active layer to bring about the pH change, have been hypothesized and limited modeled. For instance, Zhang et al. [22] coupled the multi-site Langmuir charging model with the extended Donnan-steric partitioning pore model (ext-DSP model) to describe the membrane charging mechanism and transport of H^+ and OH^- -ions.

In addition to the membrane charge ionization, several research works have described morphological and structural changes of membranes due to feedwater pH variation [23–28]. Study of Kezia et al. [23] suggested that the pH variation can bring about slight membrane swelling affecting the membrane thickness and pore size due to water uptake. This phenomenon brings about a change in water flux as well as salt rejection. Similar findings were also reported by Freger [24] for nanofiltration membranes. However, RO membranes are considered to be more rigid and thus have an insignificant swelling [24–28]. Therefore, our work did not consider the aforementioned effects and how they influence ion transport and rejection.

In the present work, we aim to investigate the effect of feedwater pH on membrane chemistry, permeate pH and rejection of ions during the RO process. A one dimensional (1-D) transport model based on the extended Donnan-steric pore (ext-DSP) model as was proposed by Bowen and Mukhtar [29], is numerically computed to simulate ion transport across the PA active layer of a TFC-RO membrane. The model is coupled with H^+ and OH^- ion transport, and membrane charge ionization, where the chemical equilibria of the FGs are explicitly modelled. We finally evaluate the model prediction experimentally based on defined conditions. However, we neglect the diffusion boundary layer (DBL), commonly known as the concentration polarization layer, on either side of the membrane so as to simplify the numerical computations of transport theory. The objective of this work is not only to observe the resulting change in membrane rejection and permeate pH, but to also gain theoretical insight on how membrane charge density, ion concentrations, and flux components vary across the membrane active layer with pH change.

2. Theory

In this section, we describe a theoretical modeling framework for ion transport and showcase how the feedwater pH affects ion rejection. Firstly, we develop a 1D transport model based on the ext-DSP model to explain steady state ion transport across the active PA toplayer in a TFC-RO membrane. We investigate transport of four ions, Na^+, Cl^-, H^+, and OH^-, across the membrane active layer (1-D) and neglect ion-ion interactions and the DBL. Secondly, a description of the membrane charge ionization as well as its interaction with H^+ and OH^- are presented. Finally, a detailed iteration step is performed with our model to fit the acid-base dosing experimental data.

2.1. Modeling ion transport through RO membrane

The transport theory is described on the basis of the ext-DSP model. The theory makes use of the extended Nernst-Planck Equation (ext-NPE) to describe the flux of ionic species through the RO membrane. The flux includes convection, diffusion, and migration transport components [30], and we take into account the friction between ions, water and the membrane matrix [31]. In this work, we express the ion flux as

$$j_i = K_{f,i} c_i v_f - K_{f,i} \varepsilon_e D_{\infty,i} \left(\frac{\partial c_i}{\partial x} + z_i c_i \frac{\partial \phi}{\partial x} \right), \tag{1}$$

where j_i is the ionic flux through the membrane, c_i the concentration of species, v_f the transmembrane water flow velocity per unit area of the membrane, $D_{\infty,i}$ is the bulk diffusion coefficient, and ε_e is the transport reduction factor expressed as $\varepsilon_e = p/\tau^2$, where p is the membrane porosity and τ is the pore tortuosity. The species valence is denoted as z_i, and ϕ is the dimensionless electrical potential scaled by RT/F, where R is the gas constant, T is temperature in K, and F is the Faraday constant. The position coordinate, x, runs from the feed to the permeate side of the membrane.

The interaction between ions and the membrane matrix is described using the friction factor, $K_{f,i}$. Previous studies with hydrodynamic theory [32] have defined the friction factor as either convective or diffusive hindrance factor ($K_{c,i}$ and $K_{d,i}$ respectively), and determined by relating the ion size to the membrane pore size [33–35]. In this work, we use a single hindrance factor for both convective and diffusive transport, i.e., $K_{c,i} = K_{d,i} = K_{f,i}$. If ions do not interact with the membrane matrix, the

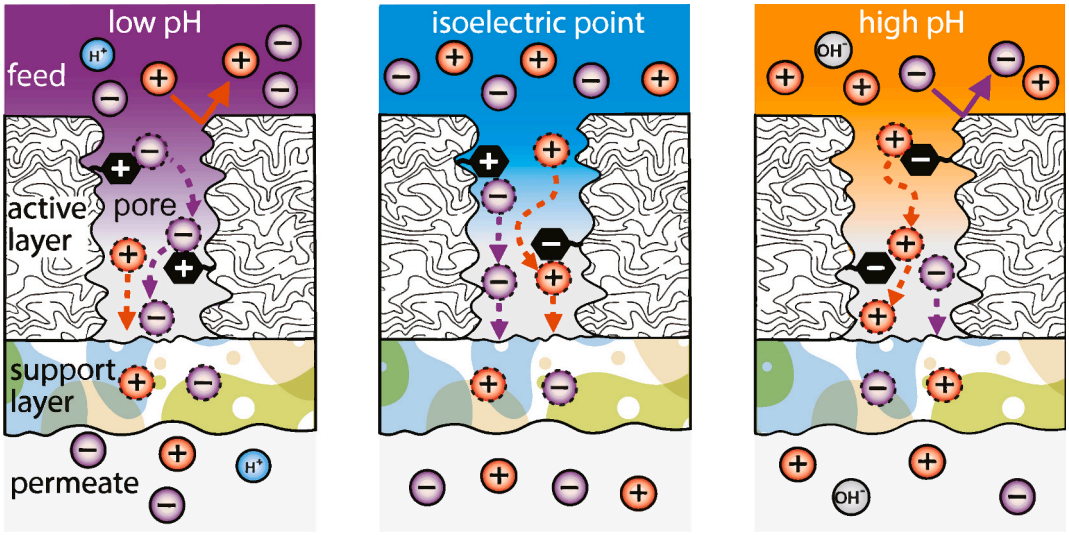

Fig. 1. Schematic depiction of pH effects on membrane charge ionization and how it affects the Donnan electrostatic exclusion (DEE) mechanism. At low pH, the membrane has a net positive charge density due to the protonation of amine groups. Cations are electrostatically repelled whereas anions are electrostatically attracted. Consequently, the reverse happens at high pH due to a net negative charge density because of deprotonation of the carboxylic groups. At isoelectric point, the membrane has a net zero charge density by which the DEE effect is cancelled out.

friction factor becomes unity, $K_{f,i} = 1$, and if they have a maximum friction with the membrane matrix, the friction factor becomes zero, $K_{f,i} = 0$. In RO systems, both cases cannot be true since it would mean that ions are either freely traversing across the membrane or they are fully retained on the feed side, respectively [31]. In this study, we assume the same $K_{f,i}$ for all ions to simplify modeling computations. A selected $K_{f,i}$ is used as a fitting parameter to describe the experimental data. We also neglect the friction due to ion-ion interactions [22,34,36].

At the membrane-water interface on either side of the active layer, ions are partitioned by the size effect (steric), charge effect (Donnan), and affinity effects (dielectric, hydrophobic attraction, etc.). These combined effects modify the bulk concentration of ions to that just within the membrane by [34,37].

$$c_{m,i} = c_{\infty,i}\Phi_i \exp(-z_i\Delta\phi_D), \tag{2}$$

where $c_{\infty,i}$ is the bulk concentration of ion in the feed or permeate side, $c_{m,i}$ is the concentration just within the membrane, $\Delta\phi_D$ is the dimensionless Donnan potential (scaled by RT/F), and Φ_i is the partitioning coefficient due to both steric and membrane affinity effects. For RO membranes, Φ_i ranges between $0 < \Phi_i < 1$ as ion-pore size ratio, and ion dehydration effects play a crucial role in transport and separation [31]. For neutral species (uncharged), the Donnan partitioning term, $e^{-z_i\Delta\phi_D}$ becomes unity and the concentration of ion just within the membrane becomes a function of only Φ_i i.e., $c_{m,i}/c_{\infty,i} = \Phi_i$.

In this study, we assume the same Φ_i for Na^+, Cl^- and use it as a fitting parameter because of insufficient qualitative data of the dehydrated ion size inside the membrane during partitioning [37–39]. This partitioning coefficient is tuned to fit the model with experimental data. Also, when investigating transport of ions, whose sizes are too small (compared to other ions or the membrane pore), the contribution of both steric and dielectric hindrances are usually smaller than the Donnan partitioning contribution [23]. Therefore, we assume that the ion sizes of H^+ and OH^- are smaller compared to those of Na^+ and Cl^- and equate their partitioning coefficients to unity, i.e., $\Phi_{H^+} = \Phi_{OH^-} = 1$. This assumption can be considered useful since having a lower than unity Φ_i for H^+ and OH^- would change the pK_a of water self-ionization reaction.

We consider local electroneutrality (EN) and zero electric current conditions at every position in the membrane, where the calculation of concentration and fluxes runs over all ions in the electrolyte, according to [40,41].

$$\sum_i z_i c_{m,i} + X_m = 0, \tag{3}$$

$$\sum_i z_i j_i = 0, \tag{4}$$

where X_m is the membrane charge density (mol/m^3), which can be constant or variable due to chemical interactions between ions and membrane matrix. This work defines the membrane charge density as a function of local pH as discussed in detail in the next subsection. Electroneutrality is also observed on the feed and the permeate sides.

For a steady state system, mass conservation of ion species is observed inside the membrane and is given by [34,42].

$$\frac{\partial j_i}{\partial x} = R_i \tag{5}$$

where R_i is the reaction rate. For ions traversing the membrane without being involved in chemical reactions (inert ions), $R_i = 0$, and Eq. (5) is reduced to $\partial j_i/\partial x = 0$, which is combined with Eq. (1) to give

$$K_{f,i}v_f\frac{\partial c_i}{\partial x} - K_{f,i}\varepsilon_e D_{\infty,i}\frac{\partial}{\partial x}\left(\frac{\partial c_i}{\partial x} + z_i c_i\frac{\partial \phi}{\partial x}\right) = 0. \tag{6}$$

Since the membrane charge ionization is a function of local pH, both H^+ and OH^- are involved in a chemical reaction expressed as

$$H_2O \leftrightharpoons H^+ + OH^-. \tag{7}$$

The concentration of H^+ and OH^- ions are related by

$$K_{eq,w} = [H^+]\cdot[OH^-], \tag{8}$$

where $K_{eq,w} = 10^{-8}$ (mM)^2 is the equilibrium constant, and [..] is the concentration (equivalent to the symbol c_i) and expressed in mM (mol/m^3). In the frame of equilibrium approach, where the reaction rates are not prescribed [43], the mass balance equations for H^+ and OH^- ions can be employed to calculate the reaction rates, i.e.,

$$\frac{\partial j_{H^+}}{\partial x} = R_{H^+}, \text{ and } \frac{\partial j_{OH^-}}{\partial x} = R_{OH^-}. \tag{9}$$

Note that the fluxes of H^+ and OH^- ions vary with position across the membrane thickness in contrast to the fluxes of inert ions (Na^+ and Cl^-), which are constant. The Nernst-Planck Eq. (1) for H^+ and OH^- ions can be combined with Eq. (8) to give the following relation

$$K_{eq,w}K_f v_f\left(D_{\infty,H^+} + D_{\infty,OH^-}\right) - D_{\infty,OH^-}[OH^-]j_{H^+} - D_{\infty,H^+}[H^+]j_{OH^-} = 0, \tag{10}$$

where we assume the same friction factor, K_f for both ions to simplify model computations and reduce the number of fitting parameters. The derivation of Eq. (10) is described in the Supporting Information (SI). To the best of our knowledge, relation (10) has not been reported in literature before, so it is derived for the first time in the present work. Note that it is valid not only for a binary aqueous electrolyte, but for a multicomponent aqueous ionic mixture as well. Equation (10) can be combined with zero current condition, Eq. (4), and Eq. (8) to give

$$j_{H^+} = \frac{K_{eq,w}K_f v_f\left(D_{\infty,H^+} + D_{\infty,OH^-}\right) - D_{\infty,H^+}[H^+](z_+j_+ + z_-j_-)}{D_{\infty,H^+}[H^+] + D_{\infty,OH^-}K_{eq,w}/[H^+]}. \tag{11}$$

Flows along the membrane are neglected, i.e., we have a dead-end geometry, so the concentration of ions on the permeate side is expressed as a function of the ion flux (j_i) and given by [22,42].

$$c_{p,i} = \frac{j_i}{v_f} \tag{12}$$

where $c_{p,i}$ is the permeate concentration. Equation (12) can only be used for inert ions, or for groups-of-ions [42], not for reactive ions such as H^+ or OH^- individually. The assumption made for Eq. (12) is useful for low water recovery (WR) investigations, (WR $= \phi_{v,p}/\phi_{v,f}$, where $\phi_{v,p}$ and $\phi_{v,f}$ are permeate and feed volumetric flow rates respectively in m^{3}s^{-1}). This is applicable for our study where WR~1% [34]. Further details on the mathematical model and its solution procedure can be found in the SI.

The reference Péclet number, Pe_{ref}, used to express the ratio of convective transport over diffusive transport [44] is defined as

$$Pe_{ref} = \frac{v_f\delta_m}{\varepsilon_e D_{ref}} \tag{13}$$

where δ_m is the membrane thickness, and D_{ref} is the reference diffusion coefficient, $D_{ref} = 1{\cdot}10^{-9}$ m^{2}s^{-1} which is ideal in our modeling as it prevents us from defining the specific Péclet number for each ion. Eq. (13) is used for our transport modeling, where several parameters are mathematically related with this one term. The typical thickness of selective layer for our modeled RO membrane is estimated as 200 nm [14,45,46].

It is important to point out that this work does not consider effect of the DBL, commonly known as the concentration polarization layer. This is because H^+ transport needs to be modeled for the DBL and it is not yet known if the pH will increase or decrease across this layer. However, the DBL can be included for a 1:1 salt or a neutral solute at a constant feed pH across the DBL thickness as summarized in Ref. [41]. By assuming high membrane retentions, i.e. $c_{f,i} \gg c_{p,i}$, a description of the concentration just outside the membrane on the feed side is given by [31,47].

$$c^{*}_{f,i} = c_{f,i} exp\left(v_f \,/\, k_{DBL,i}\right) \tag{14}$$

where $c_{f,i}$ and $c^{*}_{f,i}$ are the ion concentration in the bulk and just outside the membrane on the feed side, respectively, and $k_{DBL,i}$ is the mass transfer coefficient of an ion in the DBL, which is given by $k_{DBL,i} = \varepsilon_s D_{\infty,i}/\delta_{DBL}$ where δ_{DBL} is the DBL thickness, and ε_s is the porosity-tortuosity reduction factor due to the presence of the feed spacer. The mass transfer coefficient can be approximated using the Sherwood correlation [48,49]. Using our experimental conditions, we estimated this thickness to be about $\delta_{DBL} \sim 21$ μm and a concentration polarization modulus of 1.33 as shown in the supporting information (SI). These values are typical for spiral wound RO membranes [50].

Finally, with the ion concentrations on the permeate known, the ion rejection, R_i is computed by

$$R_i = 1 - \frac{c_{p,i}}{c_{f,i}}. \tag{15}$$

2.2. Modeling ionization of the functional groups

In this sub-section, we describe the model for ionization of membrane functional groups (FGs) (Fig. 1). The two main FGs (amine and carboxylic groups) are modeled using the chemical equilibrium relation. With the protonation of the amine groups i.e., $R\text{-}NH_3^+ \leftrightharpoons H^+ + R\text{-}NH_2$, the chemical reaction is described using a defined equilibrium constant together with the concentration of amine groups at a specified pH. This is mathematically expressed as

$$K_{eq,R\text{-}NH_2} = \frac{[H^+]\cdot[R\text{-}NH_2]}{[R\text{-}NH_3^+]}, \tag{16}$$

where $K_{eq,R\text{-}NH_2}$ is the chemical equilibrium constant of the protonated amine groups ($R\text{-}NH_3^+$), and R is the polymer backbone. The value of $K_{eq,R\text{-}NH_2}$ can be calculated from a selected pK_a value of $R\text{-}NH_3^+$, i.e., $K_{eq,R\text{-}NH_2} = 10^{-pK_{R\text{-}NH_3^+}}$. Because the amine groups have a fixed number i.e., $[R\text{-}NH_2]^{total} = [R\text{-}NH_2] + [R\text{-}NH_3^+]$, Eq. (16) becomes

$$[R\text{-}NH_3^+] = \frac{[R\text{-}NH_2]^{total}}{1 + K_{eq,R\text{-}NH_2}/[H^+]}. \tag{17}$$

Similarly, the chemical reaction for the deprotonation of the carboxylic groups, i.e., $R\text{-}COOH \leftrightharpoons H^+ + R\text{-}COO^-$, is described using a defined equilibrium constant together with the concentration of carboxylic groups at a specified pH. This is mathematically expressed as

$$[R\text{-}COO^-] = \frac{[R\text{-}COOH]^{total}}{1 + [H^+]/K_{eq,R\text{-}COOH}}, \tag{18}$$

where $K_{eq,\,R\text{-}COOH}$ is the chemical equilibrium constant of the ionized carboxylic groups ($R\text{-}COO^-$). The value of $K_{eq,\,R\text{-}COOH}$ can be calculated from a selected pK_a value of R-COOH. Past and recent studies done for the quantification of FGs concluded that ionized amine groups can be described using a single distribution (one equilibrium constant), whereas the complete ionization of carboxylic groups can be accurately modeled using a bimodal distribution (two equilibrium constants) [11,14,51–53]. Two main hypotheses have been put forward to explain the existence of this bimodal distribution. One interpretation is that two distinctly different dielectric environments exist in the polyamide film. It is attributed to the bimodal pore size distribution that has been shown to occur using Positron Annihilation Lifetime Spectroscopy analysis [54]. It is well known that the dielectric constant of water in nanopores depends on the nanopore size, which defines the degree of the equilibrium constant shift [53]. Another hypothesis is that the equilibrium constant is defined by the location of the carboxylic group within the polymer structure. The highest equilibrium constant (low pK_a) corresponds to the carboxylic groups located on the surface of the polymer structure, whereas the lowest equilibrium constant (high pK_a) corresponds to the groups located deep within the membrane matrix [11].

The total membrane charge density, X_m is expressed as $X_m = [R\text{-}NH_3^+] - [R\text{-}COO^-]_1 - [R\text{-}COO^-]_2$. Therefore, assuming a fixed number of functional charging groups in the membrane, the charge density at any position in the membrane active layer as a function of pH can be expressed as

$$X_m = \xi\left(\frac{[R\text{-}NH_2]^{total}}{1 + K_{eq,R\text{-}NH_2}/[H^+]} - \frac{[R\text{-}COOH]_1^{total}}{1 + [H^+]/K_{eq,R\text{-}COOH_1}} - \frac{[R\text{-}COOH]_2^{total}}{1 + [H^+]/K_{eq,R\text{-}COOH_2}}\right) \tag{19}$$

where ξ is the charge reduction coefficient which is introduced as a fitting parameter, $K_{eq,R\text{-}COOH_1}$, $K_{eq,R\text{-}COOH_2}$, $[R\text{-}COOH]_1^{total}$ and $[R\text{-}COOH]_2^{total}$ are the equilibrium constants and total concentrations of functional groups, respectively, of the two types of carboxylic acids present in the interfacially polymerized PA layer.

3. Materials and methods

In this section, we present the experimental approach used to investigate the performance of an RO membrane as a function of the feedwater pH during the RO process. The pH was varied using two techniques: (I) acid-base dosing technique in which acid or base was added to the feedwater solution, and (II) gas bubbling (bicarbonate system) in which the CO_2 partial pressure was varied in the electrolyte. These techniques are explained in detail in the subsections below.

3.1. Reverse osmosis membranes and pretreatment

Three experimental sets were conducted for this work. For each set, 2 flat sheet membrane cells connected in series were used. So, in total 6 experimental runs were done where the performance of 6 RO membrane pieces tested. Each piece measured $\sim$ 19.7 cm (length) by $\sim$ 12.7 cm (width), i.e., a total active surface area of $\sim$ 250 cm^2. Membranes were cut from different parts of membrane sheets obtained from a BW30HR-440 membrane module (DuPont™ FilmTec™, USA). Before each experimental run, each membrane piece was put into the stainless-steel membrane cell (homemade) together with the feed spacer (~711 μm thickness) from the same module. For each run, the membrane was hydrated with demi water for at least 12 h (overnight), and subsequently pressurized at 10 bar for 4 h. After that, the membrane was used for the pH variation experiments.

3.2. Experimental setup

All RO experiments were performed on the experimental setup described in detail in our previous work [55]. This setup consists of a crossflow filtration system (Convergence Inspector Colossus, The Netherlands), temperature control unit (FrioCell 222 Eco line, and heat exchanger), and CO_2/N_2 gas control. Novelty compared to the previous work are the addition of a second stainless steel membrane cell connected in series to the first (retentate from the first cell is feedwater for the second), and two 1 μm polypropylene filters (Van Borselen filters, The Netherlands) put in feedwater stream before the filtration pump. The purpose of filters was to reduce the risk of biological growth and particulate matter getting into the membrane cells.

3.3. Experimental conditions

Feedwater of ~30 mM NaCl was prepared in a 30 L feed tank. Besides intentional pH variations, all other experimental conditions were kept constant. Transmembrane water flux (TMF) was kept constant at TMF = 20.0 L/m^2/h (LMH) by adjusting the retentate pressure with a control valve. This pressure was around 6.2–6.8 bar, and the pressure

drop measured between the first membrane cell and after the second cell was around 0.5 bar. The feed flow rate was 50 L/h, and the permeate flow was 0.5 L/h (water recovery, WR = 1%). Since a very low WR was used, the feedwater composition for the second membrane cell can be considered to be similar to the one for the first cell. The temperature of the feedwater was maintained at ~ 25 °C using a temperature control unit (heat exchanger and a FrioCell cooling box).

3.4. pH variation

Before each experiment, a 30 mM NaCl solution was bubbled with N_2 to remove all CO_2 from the solution, and consequently, the solution pH is around 7. This solution was used as feedwater for at least 12 h (overnight) after which the samples from permeate and feed were taken. From then henceforth, feedwater pH was varied by two techniques. The first technique was by addition of acid and base. The reagents grade HCl (1.0 M and 0.1 M, VWR chemicals) and NaOH (1.0 M and 0.1 M, VWR chemicals) were added in small volumes to change the pH in low increments, with a variation range of pH 3.5–10.5. Samples under new conditions were taken after 2 h (or 12 h in case of overnight), when stationary conditions were reached (constant pH and conductivity). This process was repeated for a pH range of pH 3.5 – pH 10.5. The feed solution was replaced, and the experiment was repeated with a new membrane piece over the same pH range. Also, during experiments, feedwater was continuously bubbled with N_2 to remove the bicarbonate species, so as not to influence pH.

The second methodology for feedwater pH variation was with CO_2/N_2 gas control. This technique does not involve any acid-base dosing and is described in detail in our previous work [55]. The 30 mM NaCl feed solution is bubbled with a certain ratio of CO_2 and N_2 so that the partial pressure of CO_2 above the electrolyte is varied, and as result, the concentration of bicarbonate species, which determines the pH, is also varied. This technique enabled us to do a variation from pH 3.8–7.0. Attaining feed pH of > pH 7 using this technique is not possible with NaCl solution, but with a solution that has bicarbonate or other buffer capacities.

3.5. Sample analysis

In all experiments, 2 membrane cells connected in series were used. Separate samples were collected from the feed tank and from both cells for ion analysis (concentrations of Na^+ and Cl^- ions) using a Metrohm 930 compact ionic chromatograph (IC) with a built-in conductivity detector. The quality of analysis was checked with control samples and with Shewhart control charts, and in these reference experiments the measured concentrations were within ±5% of the calibration values. Both feed and permeate pH were measured by Orbisint CPS11D, Endress + Hauser, Switzerland. Conductivity was measured by an LTC0.35 conductivity sensor, Sensortechnik Meisenberg, Germany. Permeate flow was also measured by a mass flow meter, Cori-Flow M14, Bronkhorst, The Netherlands. The RO membrane performance, which is characterized by salt rejection was calculated by Eq. (15). Salt rejection based on conductivity was calculated from measurements of runs 1–4 and quantitatively compared with rejection chemically modeled by the OLI Studio Analyzer 3.1 as show in Fig. S.1 in the SI. The input parameters in the OLI model are the measured ion concentrations and pH. The software computes the specific electrical conductivity (mho/cm) based on these inputs. The concentration of H^+ was calculated from the measured pH values and the OH^- concentration was calculated by the H_2O equilibrium constant relation using Eq. (8). Finally, the charge balance was calculated for the permeate electrolyte. However, to ensure a zero-charge balance for runs 1–4, the permeate pH was slightly adjusted by +0.15 over the whole pH range as shown in Fig S.2 in the SI. For the experiments with bicarbonate system (runs 5 & 6), the concentration of the dissolved inorganic carbon (DIC) was calculated from the charge balance.

4. Results and discussion

In this section, we discuss in detail the rejection, and permate pH trends as functions of feed pH observed both experimentally and theoretically. We qualitatively compare the experimental data with our model predictions, only for the acid-base dosing feed pH variation, through a parametric study. The model input parameters are presented in Table 1 below. Some of these parameters were obtained from literature and from previous RO model fits. Reference and bulk diffusion coefficients (D_{ref} and $D_{\infty,i}$ respectively) for all ions investigated were obtained from previous work [42]. The total concetrations of the chemical FGs together with their respective pK_a values as quantified for FT30 RO membrane by Coronell et al. [52] were used in our numerical computations and varied for data fitting. MAPLE pre-processor enabled us to construct the transport system with a combination of chemical equilibrium reactions for charge ionization and water dissociation.

Our numerical computations involved the use of parameters defined in Table 1 for case I (values from literature), and case II (values from fitting approach with the Nelder-Mead algorithm). A detail explanation of the two cases is given in the subsection below. To validate our model, we obtained experimental data for Na^+ and Cl^- rejection as well as permeate pH at different feedwater pH (3.5–10.5). The feedwater pH was varied with HCl or NaOH dosing. Model predictions and experimental data are shown in Fig. 2 for a concentration of NaCl equal to $[NaCl]_\infty$ ~ 30 mM. It is important to also note that the feed concentration slightly varies due to the addition of either Cl^- from the HCl, or Na^+ from the NaOH during acid-base pH adjustment. This variation of the feed concentration is also incorporated into our model. However, the feed concentration of salts is kept constant for the pH variation with

Table 1
Input parameters used for our model computation. Case I values are obtained from literature whereas those for Case II are deduced from our model fitting approach.

Parameter	Value	Reference	Parameter	Value	Reference
pK_{H_2O}	14	[56]	$[R\text{-}NH_2]^{total}$	36 mM	[52]
Φ_{Na^+} , Φ_{Cl^-}	0.04 (Case I)	[47]	$[R\text{-}COOH]_1^{total}$	82 mM	[52]
	0.025 (Case II)	This work	$[R\text{-}COOH]_2^{total}$	350 mM	[52]
Φ_{H^+} , Φ_{OH^-}	1	[22,31,34]	$pK_{R\text{-}NH_2}$	4.74	[52]
$K_{f,\text{all ions}}$	0.04 (Case I)	[47]	$pK_{R\text{-}COOH_1}$	5.23	[52]
	0.025 (Case II)	This work	$pK_{R\text{-}COOH_2}$	8.97	[52]
D_{∞,Na^+} / D_{ref}	1.33	[42]	ΔpK_{FG}	0 (Case I)	[52]
D_{∞,Cl^-} / D_{ref}	2.03	[42]		0.5 (Case II)	This work
D_{∞,H^+} / D_{ref}	9.31	[42]	$\varepsilon_{e,\text{ all ions}}$	0.044 (Case I)	[38]
D_{∞,OH^-} / D_{ref}	5.30	[42]		0.027 (Case II)	This work
D_{ref}	$1{\cdot}10^{-9}$ m^2s^{-1}	[42]	ξ	1 (Case I)	[52]
v_f	5.55 m s^{-1}	This work		0.0218 (Case II)	This work

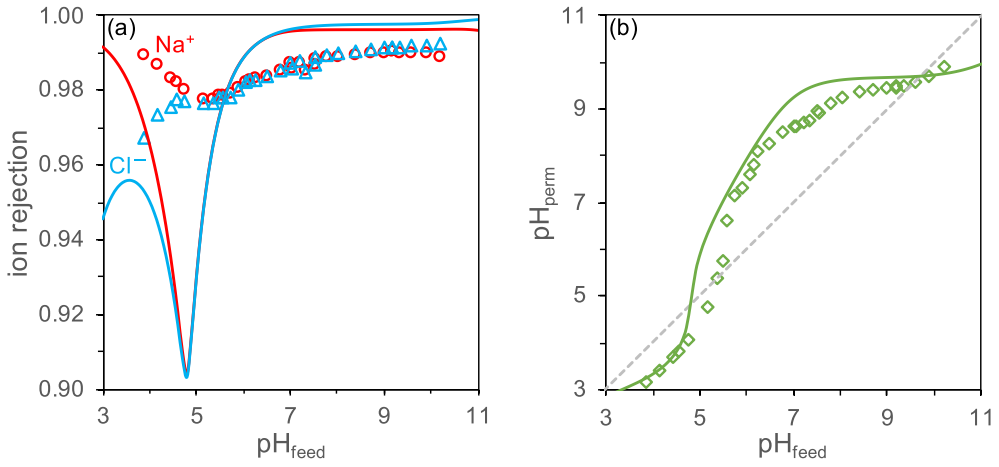

Fig. 2. Experimental (markers) and theoretical (lines) results illustrating the effect of feed pH on (a) rejection of Na^+ (red circles and line), and Cl^- (blue triangles and line), and (b) permeate pH (green diamonds and line). The dashed line depicts $pH_{permeate} = pH_{feed}$. Input model parameters are for case I. (For interpretation of the references to colour in this figure legend, the reader is referred to the Web version of this article.)

bicarbonate system. All experimental data of rejection and permeate pH as function of feed pH for the 6 runs are shown in Fig S.3 and Fig S.4 in the SI.

4.1. Model predictions and data fitting for ion rejection and permate pH

Our first numerical computation (case I) involved the use of a relatively high porosity-tortuosity reduction factor of $\varepsilon_e = 0.044$, which gives a reference Péclet number of $Pe_{ref} = 0.025$. Other parameters used for case I are listed in Table 1. As observed in Fig. 2 (a), the experimental data differs from our model prediction at low and high feedwater pH. The model predicts an isoelectric point (IEP) of 4.7 (similar to that reported by Coronell et al. [52]), which slightly differs from that obtained experimentally i.e., IEP = 5.2 ± 0.1. The underprediction of our theoretical IEP for case I might be because pH inside the membrane is slightly higher than the feed pH due to Donnan partitioning of H^+-ion at the membrane-feed interface [22]. Another reason might be the omission of H^+ partitioning due steric exclusion i.e., we assume $\Phi_{H^+} = 1$. At the IEP, the membrane has a net zero charge, as shown in Fig. 1, implying that only convection and diffusion govern transport of ions through the membrane active layer. Also, due to the zero membrane charge, partitioning on either side of the membrane surface will be dominated by steric exclusion. This explains the minimum rejection of ions as predicted by the model using Eq. (15) ($R_{Na^+} = R_{Cl^-} = 90.3\%$). However, this rejection is lower than the experimental value of 97.5± 0.1%. Above the IEP, > pH 4.8, both model predictions and the experimental data show a steady increase in rejection of both Na^+ and Cl^-. This is attributed to an increase in negative ionization of the membrane charge due to the deprotonation of the carboxylic FGs and uptake of OH^-. As a result, Donnan electrostatic exclusion (DEE) of co-ions (Cl^-) increases R_{Cl^-} [57]. To maintain electroneutrality on the permeate side, R_{Na^+} increases by that same amount. At high pH, > pH 7, our model shows a plateau region where rejection of both ions is unchanged. This means that most carboxylic groups have deprotonated and any further ionization does not greatly influence rejection of ions. However, our model over-predicts rejection of both Na^+ and Cl^- at high feed pH. This might be due to the high concentration of the deprotonated carboxylic functional groups.

At high feedwater pH, i.e., > pH 9.5, experimental data shows a slight drop in R_{Na^+} and a corresponding slight increase in R_{Cl^-}. This might be attributed to an increase in the amount of Na^+-ions in the feed from NaOH dosing. Due to this high concentration of Na^+ in the feed, more Na^+ will be transported from the membrane feed side to the permeate side, thus lowering R_{Na^+}. Also, further deprotonation of the carboxylic groups will increase the net negative charge density, thus increasing R_{Cl^-}.

Similarly, below the IEP, the model predicts a higher increase in R_{Na^+} as compared to R_{Cl^-}. This is not in line with the experimental data which shows a further decrease in R_{Cl^-}. At this low pH, the membrane becomes positively charged due to the protonation of the amine FGs. The donnan electrostatic repulsion of the co-ions (Na^+) increases R_{Na^+}. The difference in rejection between Na^+ and Cl^- means that H^+-ions traverse the membrane from the feed side to the permeate side to maintain electroneutrality [23]. This rejection trend at low pH is also confirmed in Ref. [13].

Fig. 2(b) shows permeate pH as a function of feed pH. The prediction shows a negative rejection of H^+ at feed pH < IEP and at feed pH > pH 9.5. The negative rejection at low pH (<IEP) is due to transport of H^+-ions from the feed side to the permeate side as previously described. This transport is driven by a negative *trans*-membrane potential as shown in Fig. S.5 in the SI. Conversely, above the IEP, permeate pH is higher than feed pH due to the positive *trans*-membrane potential developed across the membrane thickness, which increases rejection of H^+-ions. The positive potential is brought about by the reduction of Na^+ flux and an increase in Cl^- flux to bring about zero net charge flux [22].

To have a best model fit (case II), we performed a parametric study with Nelder-Mead fitting approach [58] (part of the study is shown in section 5 of the SI), where we lowered our porosity reduction factor to $\varepsilon_e = 0.027$, which increased the reference Péclet number to $Pe_{ref} = 0.041$. The increase of Pe_{ref} ensured a reduction in the rejection dip at the IEP. We also varied other parameters including the partitioning coefficient, friction factor, and the total concentrations of the chemical FGs as reported by Coronell et al. ([52], our Table 1), since they are not defined per unit aqueous phase in the polyamide active layer [34]. Finally, we introduced a pK_a shift parameter for the membrane FGs, denoted as ΔpK_{FG}. This parameter shifts the theory line to the right so as to fit the experimental data. However, it is crucial to note that the new values (pK^*_{FG}), i.e., $pK^*_{FG} = pK_{FG} + \Delta pK_{FG}$ might not the real values for a BW30HR-440 RO membrane. The real pK_{FG} values should be experimentally determined by titration. A qualitative comparison of experimental data with the new model prediction is shown in Fig. 3.

As already mentioned above, the parametric study shows that for a proper data fit, all transport modeling parameters i.e., reduction factor due to porosity-tortuosity, partitioning coefficients, and friction factors should be lowered further. Computations done with these new fitting parameters compare well with the data for rejection, Fig. 3(a), and permeate pH, Fig. 3(b), which clearly indicates that our membrane has a very dense polyamide active layer with a low surface charge density. A

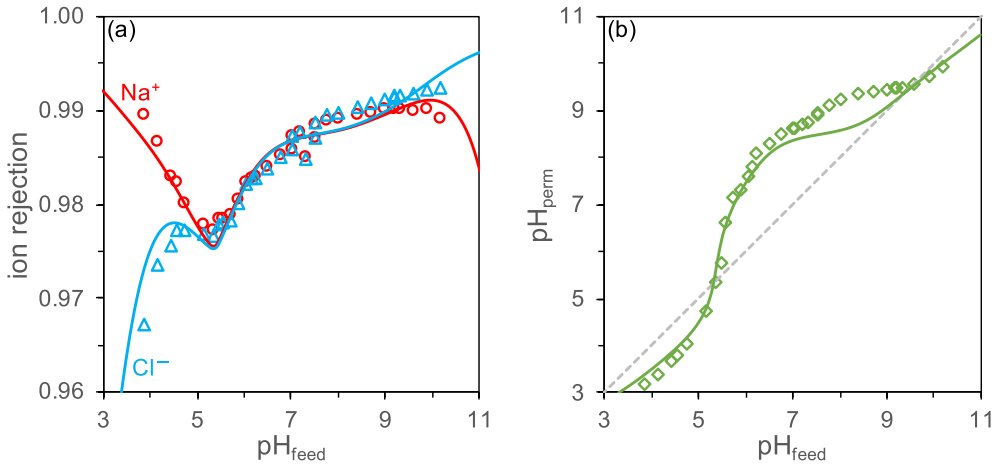

Fig. 3. Experimental (markers) and theoretical (lines) results illustrating effect of feed pH on (a) rejection of Na^+ (red circles and line), and Cl^- (blue triangles and line), and (b) permeate pH (green diamonds and line). The dashed line depicts $pH_{permeate} = pH_{feed}$. Modified input model parameters are for case II. (For interpretation of the references to colour in this figure legend, the reader is referred to the Web version of this article.)

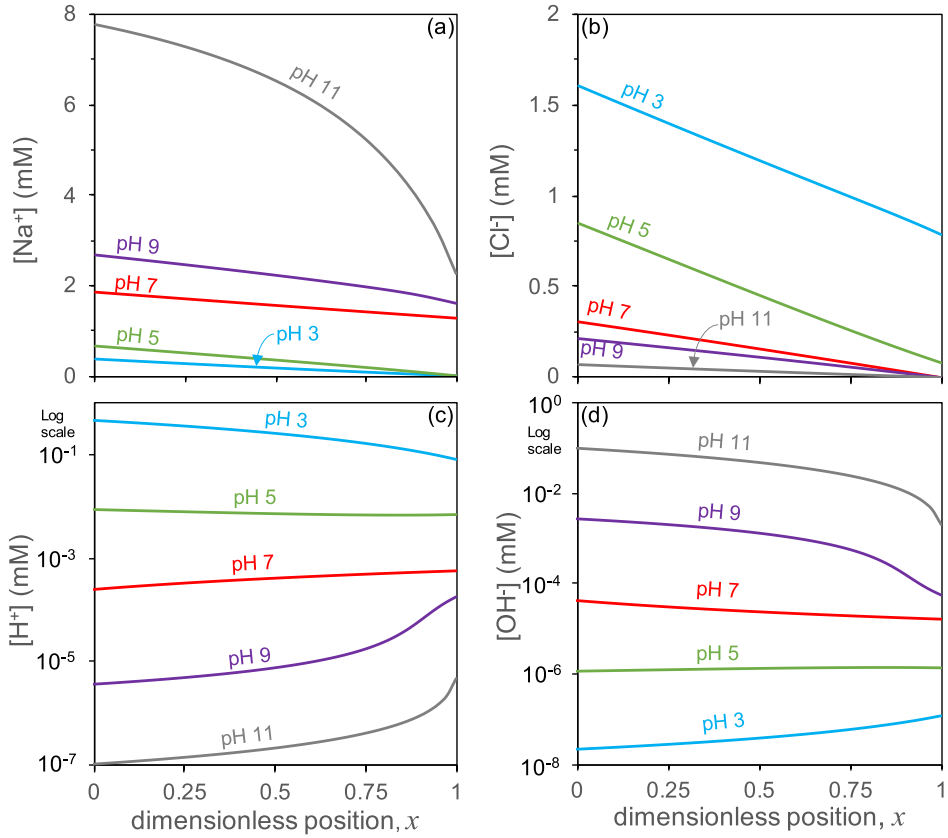

Fig. 4. Theoretical concentration profiles of (a) Na^+, (b) Cl^-, (c) H^+, and (d) OH^- with pH variation as functions of dimensionless position, x, across the membrane active layer thickness. Input model parameters are for case II.

possible reason for the low porosity reduction factor could be the absence of the DBL in our model. The fit also proves that indeed the membrane charge is a function of local pH, as described in the theory section 2.

4.2. Profiles across the membrane

Apart from rejection and permeate pH, profiles of ion concentration, flux, membrane charge density, and electrical potential were modeled across the membrane active layer thickness. We neglected the diffusion boundary layer (DBL), and the ion-ion interactions, which was modeled in our previous work [42]. Fig. 4(a) shows a gradual increase in the concentration of Na^+ inside the membrane with a corresponding increase in pH. This is because of the DEE mechanism, which allows the attraction of the counter-ions (Na^+) and a corresponding repulsion of co-ions (Cl^-) as observed in Fig. 4(b). However, concentrations of both Na^+ and Cl^- drop across the membrane thickness, i.e., from $x = 0$ to $x = 1$, due to the membrane charge effect which brings about the DEE and also the electroneutrality conditions at each position inside the membrane [42].

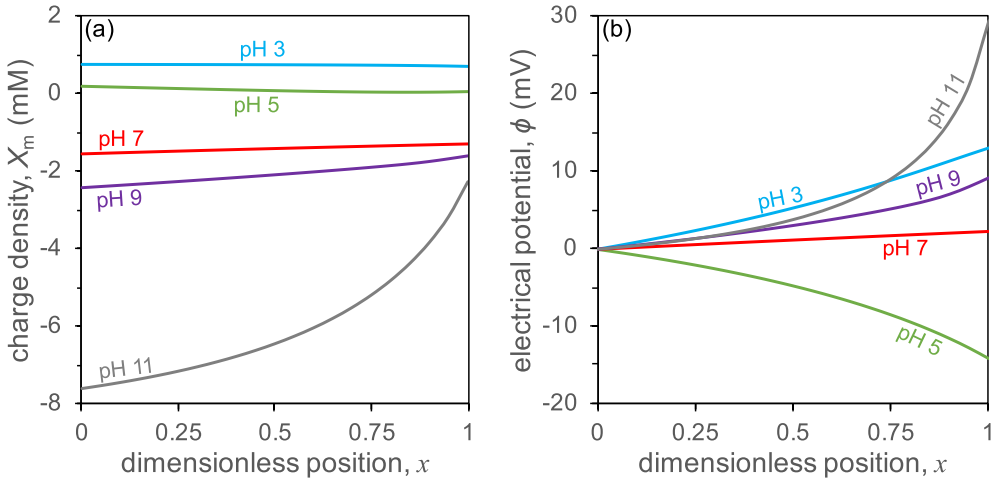

Fig. 5. Profiles of (a) membrane charge density in mM, and (b) membrane electrical potential in mV, as functions of dimensionless position, x, across the membrane active layer thickness. Input model parameters are for case II.

The concentration profiles for H^+, Fig, 4(c), and OH^-, Fig. 4(d) typically mirror each other. At low pH, the protonation of the amine groups will lead to an uptake of H^+ -ions thus decreasing their concentration across the membrane thickness. Consequently, above the IEP, the deprotonation of carboxylic FGs will result into an uptake of OH^--ions and therefore a decrease in concentration across the membrane thickness [27].

At every position across the active layer thickness, the membrane charge density is a function of local pH as shown in Fig. 5(a). The charge density gradually decreases across the active layer thickness, i.e., from feed side ($x = 0$) to permeate side ($x = 1$), for pH < IEP. The membrane is positively charged at pH < IEP due to the protonation of the amine FGs. As feedwater pH increases, at pH > IEP, the membrane becomes negatively charged due to the deprotonation of the carboxylic FGs, and the negative charge at a given location in the membrane increases with increasing pH. For our modeling pH range, our prediction shows the highest increase at pH 11. The gradual decrease trend of membrane charge across the RO membrane toplayer suggest that evaluation of the membrane charge can be done on the feed side, the permeate side, or averaged across the membrane thickness.

At high feedwater pH (pH > IEP) the membrane charge density, Fig. 5 (a), and electrical potential, Fig. 5(b) display a typical behaviour for a polyamide layer where both the negative charge density and electrical potential increases with feed pH [23]. The electrical potential for a negatively charged membrane increases across the membrane in the direction of ion flux, i.e., from $x = 0$ to $x = 1$. Because the salt concentration in the feed is relatively higher than that of H^+ and OH^-, both membrane charge density and electrical potential inside the membrane are greatly determined by the salt ions traversing the membrane [22]. The transport of salt across the membrane also determines the transmembrane electrical potential. The positive transmembrane electrical potential at higher pH is due to the presence of more counter-ions (Na^+) in the membrane, Fig. S.5. This results in the reduction of Na^+ flux and an increase in Cl^- flux so as to bring about zero charge flux [38].

4.3. Charge density as a function of feedwater pH

In order to better understand the pH effects on membrane surface charge, we need to analyze the charging curves for the membrane charge density on either side of the membrane (feed and permeate) as functions of feed pH. Fig. 6 shows the two profiles, in which the surface charge on the feed side greatly varies with increasing feed pH. This does indicate that quantification of the membrane charge density is better described on the feed side as is also confirmed by the average surface charge plot

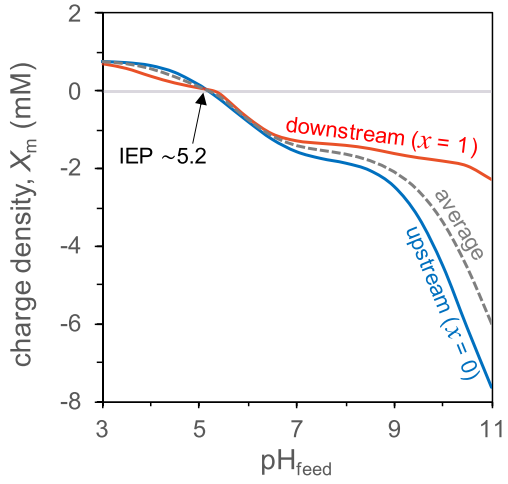

Fig. 6. Profile of membrane charge density, X_m in mM as a function of feed pH computed for the membrane surface on the upstream side, $x = 0$, (blue line), on the downstream side, $x = 1$, (red line), and average throughout the membrane thickness, (grey dashed line). The net membrane charge density at IEP ~ 5.2, $X_m = 0$ mM. The modeling parameters are for case II. (For interpretation of the references to colour in this figure legend, the reader is referred to the Web version of this article.)

(grey dashed line), where charge density on the feed side accounts for the highest percentage of the average surface charge. The total membrane charge computed in this work is quite low in comparison with the one quantified by Corronell et al. [52]. This might be due to the complexation of the ionized surface charge with Na^+ and Cl^- ions at high and low feed pH respectively i.e., $R\text{-}COO^- + Na^+ \rightleftharpoons R\text{-}COO^-Na^+$ and $R\text{-}NH_3^+ + Cl^- \rightleftharpoons R\text{-}NH_3^+Cl^-$. These ions might have been adsorbed by the ionized FGs as was reported in Refs. [22,59]. The ion complexation effects are not taken into account in this work. Conversely, the low charge density could mean that our membrane has a weakly charged dense polymer film, with ion rejection being dominated by steric and dielectric partitioning, as was also reported by Stolov et al., [27]. In general, we conclude that the effective membrane charge is actually less than what would be measured by titration. This conclusion can be validated by membrane charge measurement using the titration technique, which was not done in this work due to the complexity in sublayer charge measurement.

Finally, to confirm that a polyamide layer is indeed slightly charged

below and above the IEP, we performed a check by setting the membrane charge to zero ($X_m = 0$). We numerically computed ion rejection and permeate pH as functions of feed pH using modeling parameters for case II. We also varied the diffusion coefficient of cation (Na^+) to check for fitting with the experimental data as shown in Fig S.7 in the SI. We observed a clear difference between experimental data and theory lines. The model predictions for all three diffusion coefficients show a gradual decrease and increase in rejections of Na^+ and Cl^- respectively with pH increase, Fig S.7 (a). Profiles of permate pH as functions of feed pH, Fig S.7 (b), also show a disagreement between experimental data and theory lines. All three theory lines show a trend where $pH_{permeate} \cong pH_{feed}$ for all pH ranges. We therefore conclude that polyamide membranes are indeed weakly charged, but this small charge plays a key role in transport and rejection of ions.

4.4. Transport component description across the membrane

We also investigate the contribution of each transport mechanism (convection, diffusion, and electromigration) to the total flux of ions through the membrane thickness at low and high feedwater pH (pH 3, and pH 9 respectively). As observed in Figs. 7 and 8, transport of all ions i.e., Na^+, Cl^-, H^+, and OH^- at low concentration and low Péclet number ($Pe < 1$) is dominated by diffusion [22,37]. For all cases, convection accounts for the lowest percentage of overall transport. Since we consider a steady-state transport description, and assume that Na^+ and Cl^- ions are non-reactive, by virtue of electroneutrality, their total fluxes at the two pH conditions are constant throughout the membrane thickness [60] as shown in Fig. 7. At pH 3, the flux of Cl^- is higher than that of Na^+ due to the positive charge of the membrane, which allows more Cl^- to pass through, while restricting passage of Na^+ by the DEE mechanism. Consequently, the opposite is observed at pH 9, where Na^+ has a higher flux as compared to Cl^-.

For H^+ and OH^-, the total fluxes vary with position across the membrane thickness according to Eq. (10) and Eq. (11) and are shown in Fig. 8. At pH 3, the total proton flux is highest and appears constant across the membrane thickness (Fig. 8(a)), whereas the total flux of OH^- is negative and decreases across the membrane thickness (Fig. 8(b)). The negative flux of OH^- at low pH means that OH^- ions traverse the membrane in the opposite direction, i.e., from the permeate to the feed side thus lowering the permeate pH. This opposite flux phenomenon is due to the negative transmembrane potential that develops for a positively charged membrane to ensure a decrease of OH^- flux and therefore maintaining a zero membrane current [22]. At pH 9, the reverse happens, where H^+ total flux is negative (Fig. 8(c)) and that of OH^- is positive (Fig. 8(d)) thus increasing the permeate pH. We also observe a drop of total flux for both H^+ and OH^- on the permeate side ($x = 1$). This is due to the backward reaction (association) of H^+ and OH^- to form H_2O as expressed by Eq. (7).

5. Conclusion

This study focused on investigating the effects of feedwater pH on membrane charge ionization, rejection of ions, and permeate pH. We modeled the protonation of the amine groups together with the deprotonation of the carboxylic groups at low and high pH, respectively. We present a theoretical modeling framework, which can predict the ion rejection, permeate pH, and the profiles of ion concentration, membrane charge density, and flux components across the membrane active layer. The theory follows the classical approach, which describes the ionization of amine groups with one equilibrium constant and that of carboxylic groups with bimodal equilibrium constant. The model is fitted with experimental data obtained by desalination of 30 mM NaCl and pH

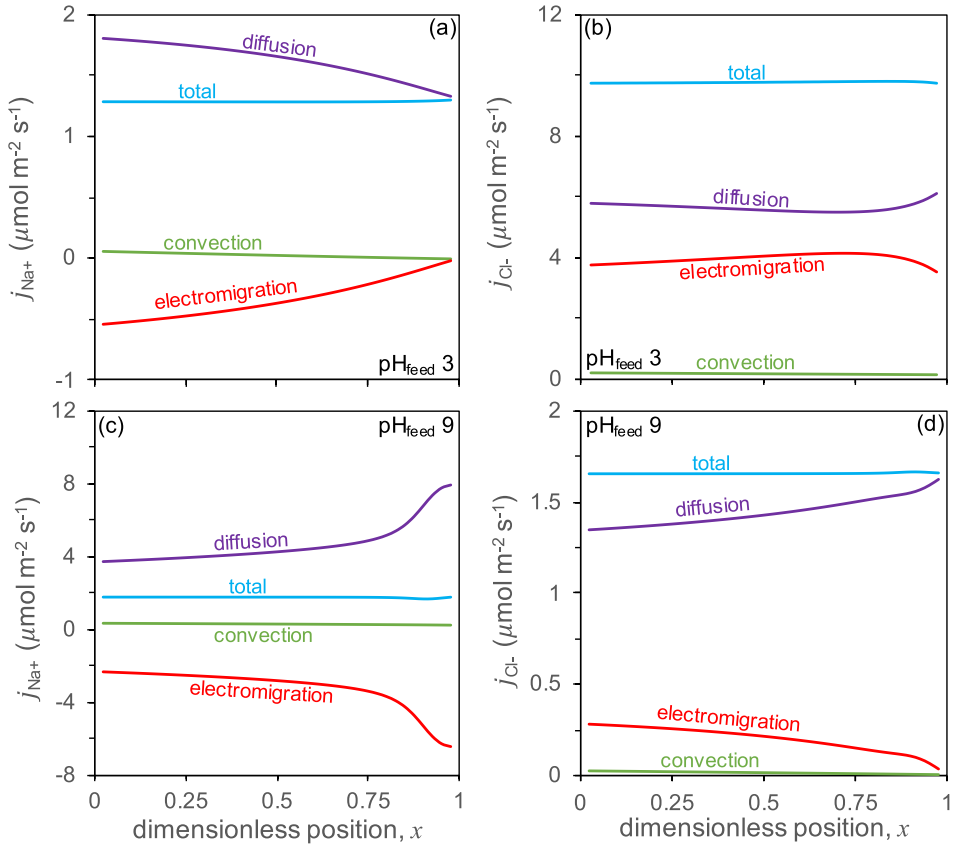

Fig. 7. The profiles of Na^+ and Cl^- fluxes and their components due to diffusion, convection, and electromigration at pH 3 (a, b), and pH 9 (c, d) as functions of dimensionless position, x, across the membrane thickness. The modeling parameters are for case II.

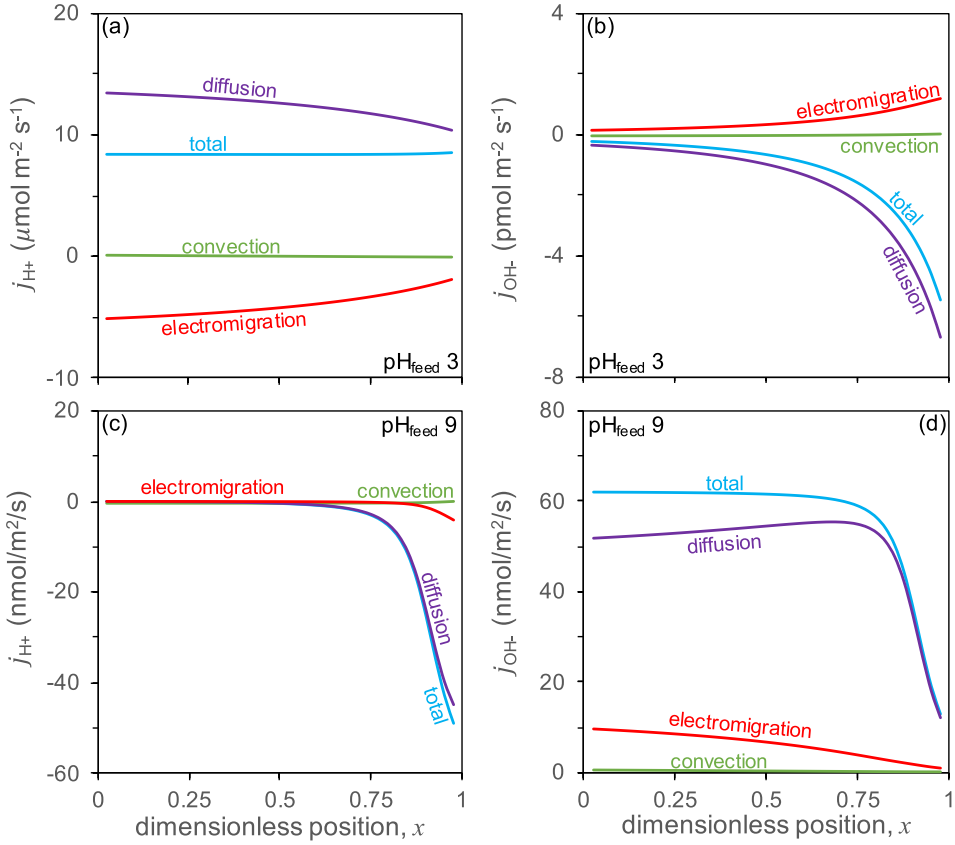

Fig. 8. The profiles of H^+ and OH^- fluxes and their components due to diffusion, convection, and electromigration at pH 3 (a, b) and pH 9 (c, d) as functions of dimensionless position, x, across the membrane thickness. The modeling parameters are for case II.

variation with HCl and NaOH. To obtain a good model fit, a parametric study was conducted by adjusting the fitting parameters such as the porosity-tortuosity reduction factor, and the membrane charge reduction coefficient. Both theory and experiment show a clear trend in rejection of Na^+ and Cl^-, where they diverge at low and high feedwater pH. Also, the permeate pH shows a variation with feed pH. This is due to the membrane being charged positive at low pH and negative at high pH. We also theoretically illustrate that for a system of only monovalent ions, the membrane charge is a function of local pH as it gradually reduces across the membrane active layer thickness. The reduction is highest at pH 11. Our results clearly show that the polyamide layer is only slightly charged, but this small charge still plays an important role to determine salt rejection. Thus, with this study, we provide an extensive description of the physical-chemical processes that happen during RO processes at a wide feedwater pH range. Our model description can be further extended to include more ions and acid-base reactions that occur during desalination of multicomponent mixtures.

Author statement

All authors contributed equally to this work.

Declaration of competing interest

The authors declare that they have no known competing financial interests or personal relationships that could have appeared to influence the work reported in this paper.

Data availability

The research data underlying this work is available at https://doi.org/10.4121/20160329.

Acknowledgements

This work was performed in the cooperation framework of Wetsus, *European Centre of Excellence for Sustainable Water Technology* (www.wetsus.nl). Wetsus is co-funded by the Dutch Ministry of Economic Affairs and Ministry of Infrastructure and Environment, the Province of Fryslân, and the Northern Netherlands Provinces. The authors thank the participants in the Wetsus research theme "Advanced Water Treatment", for fruitful discussions and financial support.

Appendix A. Supplementary data

Supplementary data to this article can be found online at https://doi.org/10.1016/j.memsci.2022.120800.

References

[1] E. Jones, M. Qadir, M.T.H. van Vliet, V. Smakhtin, S. Kang, Science of the Total Environment the state of desalination and brine production : a global outlook, Sci. Total Environ. 657 (2019) 1343–1356, https://doi.org/10.1016/j.scitotenv.2018.12.076.

[2] H.T. do Thi, T. Pasztor, D. Fozer, F. Manenti, A.J. Toth, Comparison of desalination technologies using renewable energy sources with life cycle, PESTLE, and multi-criteria decision analyses, water 13 (2021) 3023, https://doi.org/10.3390/w13213023.

[3] B. Anand, R. Shankar, S. Murugavelh, W. Rivera, K.M. Prasad, R. Nagarajan, A review on solar photovoltaic thermal integrated desalination technologies,

Renew. Sustain. Energy Rev. 141 (2021), 110787, https://doi.org/10.1016/j.rser.2021.110787.
[4] F. Esmaeilion, Hybrid renewable energy systems for desalination, Appl. Water Sci. 10 (10) (2020) 84, https://doi.org/10.1007/s13201-020-1168-5.
[5] H.C. Duong, T.L. Tran, A.J. Ansari, H.T. Cao, T.D. Vu, K.U. Do, Advances in membrane materials and processes for desalination of Brackish water, Curr. Pollut. Reports 5 (2019) 319–336, https://doi.org/10.1007/s40726-019-00121-8.
[6] Y. Yao, P. Zhang, C. Jiang, R.M. DuChanois, X. Zhang, M. Elimelech, High performance polyester reverse osmosis desalination membrane with chlorine resistance, Nat. Sustain. 4 (2021) 138–146, https://doi.org/10.1038/s41893-020-00619-w.
[7] K.P. Lee, T.C. Arnot, D. Mattia, A review of reverse osmosis membrane materials for desalination-Development to date and future potential, J. Memb. Sci. 370 (2011) 1–22, https://doi.org/10.1016/j.memsci.2010.12.036.
[8] M. Asadollahi, D. Bastani, S.A. Musavi, Enhancement of surface properties and performance of reverse osmosis membranes after surface modification: a review, Desalination 420 (2017) 330–383, https://doi.org/10.1016/j.desal.2017.05.027.
[9] D.G. Cahill, V. Freger, Microscopy and microanalysis of reverse-osmosis and nanofiltration membranes, Mater. Res. Soc. Bull. 33 (2008) 27–32, https://doi.org/10.1557/mrs2008.11.
[10] T.A. Otitoju, R.A. Saari, A.L. Ahmad, Progress in the modification of reverse osmosis (RO) membranes for enhanced performance, J. Ind. Eng. Chem. 67 (2018) 52–71, https://doi.org/10.1016/j.jiec.2018.07.010.
[11] D. Chen, J.R. Werber, X. Zhao, M. Elimelech, A facile method to quantify the carboxyl group areal density in the active layer of polyamide thin-film composite membranes, J. Memb. Sci. 534 (2017) 100–108, https://doi.org/10.1016/j.memsci.2017.04.001.
[12] M.S. Hall, V.M. Starov, D.R. Lloyd, Reverse osmosis of multicomponent electrolyte solutions. Part I. Theoretical development, J. Memb. Sci. 128 (1997) 23–37, https://doi.org/10.1016/S0376-7388(96)00300-6.
[13] M.S. Hall, D.R. Lloyd, V.M. Starov, Reverse osmosis of multicomponent electrolyte solutions. Part II. Experimental verification, J. Memb. Sci. 128 (1997) 39–53, https://doi.org/10.1016/S0376-7388(96)00301-8.
[14] O. Coronell, M.I. González, B.J. Mariñas, D.G. Cahill, Ionization behavior, stoichiometry of association, and accessibility of functional groups in the active layers of reverse osmosis and nanofiltration membranes, Environ. Sci. Technol. 44 (2010) 6808–6814, https://doi.org/10.1021/es100891r.
[15] R. Epsztein, R.M. DuChanois, C.L. Ritt, A. Noy, M. Elimelech, Towards single-species selectivity of membranes with subnanometre pores, Nat. Nanotechnol. 15 (2020) 426–436, https://doi.org/10.1038/s41565-020-0713-6.
[16] L. Malaeb, G.M. Ayoub, Reverse osmosis technology for water treatment: state of the art review, Desalination 267 (2011) 1–8, https://doi.org/10.1016/j.desal.2010.09.001.
[17] J.G. Wijmans, R.W. Baker, The solution-diffusion model: a review, J. Memb. Sci. 107 (1995) 1–21, https://doi.org/10.1016/0376-7388(95)00102-I.
[18] M. Shen, S. Keten, R.M. Lueptow, Dynamics of water and solute transport in polymeric reverse osmosis membranes via molecular dynamics simulations, J. Memb. Sci. 506 (2016) 95–108, https://doi.org/10.1016/j.memsci.2016.01.051.
[19] H. Yasuda, A. Peterlin, Diffusive and bulk flow transport in polymers, J. Appl. Polym. Sci. 17 (1973) 433–442, https://doi.org/10.1002/app.1973.070170209.
[20] W.L. Ang, A.W. Mohammad, Mathematical modeling of membrane operations for water treatment, in: Advances in Membrane Technologies for Water Treatment, Elsevier Ltd, 2015, pp. 379–407. ISBN: 9781782421269.
[21] O. Nir, N.F. Bishop, O. Lahav, V. Freger, Modeling pH variation in reverse osmosis, Water Res 87 (2015) 328–335, https://doi.org/10.1016/j.watres.2015.09.038.
[22] L. Zhang L, H.V.M. Hamelers, P.M. Biesheuvel, Modeling permeate pH in RO membranes by the extended Donnan steric partitioning pore model, J. Memb. Sci. 613 (2020), 118511, https://doi.org/10.1016/j.memsci.2020.118511.
[23] K. Kezia, J. Lee, W. Ogieglo, A. Hill, N.E. Benes, S.E. Kentish, The transport of hydronium and hydroxide ions through reverse osmosis membranes, J. Memb. Sci. 459 (2014) 197–206, https://doi.org/10.1016/j.memsci.2014.02.018.
[24] V. Freger, Swelling and morphology of the skin layer of polyamide composite membranes: an atomic force microscopy study, Environ. Sci. Technol. 38 (2004) 3168–3175, https://doi.org/10.1021/es034815u.
[25] V. Kolev, V. Freger, Hydration, porosity and water dynamics in the polyamide layer of reverse osmosis membranes: a molecular dynamics study, Polymer (Guildf). 55 (2014) 1420–1426, https://doi.org/10.1016/j.polymer.2013.12.045.
[26] X. Zhang, D.G. Cahill, O. Coronell, B.J. Mariñas, Absorption of water in the active layer of reverse osmosis membranes, J. Memb. Sci. 331 (2009) 143–151, https://doi.org/10.1016/j.memsci.2009.01.027.
[27] M. Stolov, V. Freger, Membrane charge weakly affects ion transport in reverse osmosis, Environ. Sci. Technol. Lett. 7 (2020) 440–445, https://doi.org/10.1021/acs.estlett.0c00291.
[28] E. Dražević, K. Košutić, V. Freger, Permeability and selectivity of reverse osmosis membranes: correlation to swelling revisited, Water Res 49 (2014) 444–452, https://doi.org/10.1016/j.watres.2013.10.029.
[29] W.R. Bowen, H. Mukhtar, Characterisation and prediction of separation performance of nanofiltration membranes, J. Memb. Sci. 112 (1996) 263–274, https://doi.org/10.1016/0376-7388(95)00302-9.
[30] T. Teorell, Transport phenomena in membranes, Angew. Chemie Int. Ed. English 8 (1959) 42–54, https://doi.org/10.1002/anie.196900421.
[31] P.M. Biesheuvel, S. Porada, M. Elimelech, J.E. Dykstra, Tutorial review of reverse osmosis and electrodialysis, J. Memb. Sci. 647 (2021), 120221, https://doi.org/10.1016/j.memsci.2021.120221.
[32] W.M. Deen, Hindered transport of large molecules in liquid-filled pores, AIChE J 33 (1987) 1409–1425, https://doi.org/10.1002/aic.690330902.
[33] M. Tedesco, H.V.M. Hamelers, P.M. Biesheuvel, Nernst-Planck transport theory for (reverse) electrodialysis: II. Effect of water transport through ion-exchange membranes, J. Memb. Sci. 531 (2017) 172–182, https://doi.org/10.1016/j.memsci.2017.02.031.
[34] P.M. Biesheuvel, L. Zhang, P. Gasquet, B. Blankert, M. Elimelech, W.G.J. Van der Meer, Ion selectivity in Brackish water desalination by reverse osmosis: theory, measurements, and implications, Environ. Sci. Technol. Lett. 7 (2020) 42–47, https://doi.org/10.1021/acs.estlett.9b00686.
[35] S. Bandini, D. Vezzani, Nanofiltration modeling : the role of dielectric exclusion in membrane characterization, Chem. Eng. Sci. 58 (2003) 3303–3326, https://doi.org/10.1016/S0009-2509(03)00212-4.
[36] P. Dechadilok, W.M. Deen, Hindrance factors for diffusion and convection in pores, Ind. Eng. Chem. Res. 45 (2006) 6953–6959, https://doi.org/10.1021/ie051387n.
[37] Y.S. Oren, P.M. Biesheuvel, Theory of ion and water transport in reverse-osmosis membranes, Phys. Rev. Appl. 9 (2018), 024034, https://doi.org/10.1103/PhysRevApplied.9.024034.
[38] L. Wang, T. Cao, J.E. Dykstra, S. Porada, P.M. Biesheuvel, M. Elimelech, Salt and water transport in reverse osmosis membranes: beyond the solution-diffusion model, Environ. Sci. Technol. 55 (2021) 16665–16675, https://doi.org/10.1021/acs.est.1c05649.
[39] C. Lu, C. Hu, C.L. Ritt, X. Hua, J. Sun, H. Xia, Y. Liu, D.W. Li, B. Ma, M. Elimelech, J. Qu, In situ characterization of dehydration during ion transport in polymeric nanochannels, J. Am. Chem. Soc. 143 (2021) 14242–14252, https://doi.org/10.1021/jacs.1c05765.
[40] J.E. Dykstra, K.J. Keesman, P.M. Biesheuvel, A. van der Wal, Theory of pH changes in water desalination by capacitive deionization, Water Res 119 (2017) 178–186, https://doi.org/10.1016/j.watres.2017.04.039.
[41] P.M. Biesheuvel, J.E. Dykstra, Physics of electrochemical processes, in: http://www.physicsofelectrochemicalprocesses.com, 2020. ISBN: 978-90-9033258-1.
[42] E.M. Kimani, A.J.B. Kemperman, W.G.J. van der Meer, P.M. Biesheuvel, Multicomponent mass transport modeling of water desalination by reverse osmosis including ion pair formation, J. Chem. Phys. 154 (2021), 124501, https://doi.org/10.1063/5.0039128.
[43] P.C. Lichtner, Continuum model for simultaneous chemical reactions and mass transport in hydrothermal systems, Geochim. Cosmochim. Acta 49 (1985) 779–800, https://doi.org/10.1016/0016-7037(85)90172-3.
[44] M. Huysmans, A. Dassargues, Review of the use of Péclet numbers to determine the relative importance of advection and diffusion in low permeability environments, Hydrogeol. J. 13 (2005) 895–904, https://doi.org/10.1007/s10040-004-0387-4.
[45] B. Mi, O. Coronell, B.J. Mariñas, F. Watanabe, D.G. Cahill, I. Petrov, Physico-chemical characterization of NF/RO membrane active layers by Rutherford backscattering spectrometry, J. Memb. Sci. 282 (2006) 71–81, https://doi.org/10.1016/j.memsci.2006.05.015.
[46] X. Zhang, D.G. Cahill, O. Coronell, B.J. Mariñas, Partitioning of salt ions in FT30 reverse osmosis membranes, Appl. Phys. Lett. 91 (2007), 181904, https://doi.org/10.1063/1.2802562.
[47] P.M. Biesheuvel, J.E. Dykstra, S. Porada, M. Elimelech, New parametrization method for salt permeability of reverse osmosis desalination membranes, J. Membr. Sci. Lett. 2 (2021), 100010, https://doi.org/10.1016/j.memlet.2021.100010.
[48] S. Kim, E.M.V. Hoek, Modeling concentration polarization in reverse osmosis processes, Desalination 186 (2005) 111–128, https://doi.org/10.1016/j.desal.2005.05.017.
[49] Z. Zhou, B. Ling, I. Battiato, S.M. Husson, D.A. Ladner, Concentration polarization over reverse osmosis membranes with engineered surface features, J. Memb. Sci. 617 (2021), 118199, https://doi.org/10.1016/j.memsci.2020.118199.
[50] R.W. Baker, Concentration Polarization 4.1 *Membrane Technology And Applications*, John Wiley & Sons, Ltd), 2012, ISBN 978-0-470-74372-0.
[51] C.C. Wamser, M.I. Gilbert, Detection of surface functional group Asymmetry in interfacially-polymerized films by contact angle titrations, Langmuir 8 (1992) 1608–1614, https://doi.org/10.1021/la00042a019.
[52] O. Coronell O, B.J. Mariñas, X. Zhang, D.G. Cahill, Quantification of functional groups and modeling of their ionization behavior in the active layer of FT30 reverse osmosis membrane, Environ. Sci. Technol. 42 (2008) 5260–5266, https://doi.org/10.1021/es8002712.
[53] C.L. Ritt, J.R. Werber, M. Wang, Z. Yang, Y. Zhao, H.J. Kulik, Ionization behavior of nanoporous polyamide membrane, PNAS 117 (48) (2020) 30191–30200, https://doi.org/10.1073/pnas.2008421117.
[54] S.H. Kim, S.Y. Kwak, T. Suzuki, Positron annihilation spectroscopic evidence to demonstrate the flux-enhancement mechanism in morphology-controlled thin-film-composite (TFC) membrane, Environ. Sci. Technol. 39 (2005) 1764–1770, https://doi.org/10.1021/es049453k.
[55] M. Pranić, E.M. Kimani, P.M. Biesheuvel, S. Porada, Desalination of complex multi-ionic solutions by reverse osmosis at different pH values, temperatures, and compositions, ACS Omega 6 (2021) 19946–19955, https://doi.org/10.1021/acsomega.1c02931.
[56] A.G. Dickson, J.P. Riley, The estimation of acid dissociation constants in seawater media from potentionmetric titrations with strong base. I. The ionic product of water - K_w, Mar. Chem. 7 (1979) 89–99, https://doi.org/10.1016/0304-4203(79)90001-X.
[57] O. Coronell, B. Mi, B.J. Marinas, D.G. Cahill, Modeling the effect of charge density in the active layers of reverse osmosis and nano fi ltration membranes on the rejection of arsenic(III) and potassium iodide, Environ. Sci. Technol. 47 (2013) 420–428, https://doi.org/10.1021/es302850p.

[58] J.A. Nelder, R. Mead, A simplex method for function minimization, Comput. J. 7 (1965) 308–313, https://doi.org/10.1093/comjnl/7.4.308.
[59] J.A. Davis, R.O. James, J.O. Leckie, Surface ionization and complexation at the oxide/water interface, J. Colloid Interface Sci. 63 (1978) 480–499, https://doi.org/10.1016/s0021-9797(78)80009-5.
[60] V.V. Nikonenko, K.A. Lebedev, S.S. Suleimanov, Influence of the convective term in the Nernst-Planck equation on properties of ion transport through a layer of solution or membrane, Russ. J. Electrochem. 45 (2009) 160–169, https://doi.org/10.1134/S1023193509020062.